Experiments conducted at the University of Tsukuba

Porous silicon films. Magnetic domain walls are generating significant interest in the field of spintronics, predominantly for potential applications in data storage, data processing and "memristive" devices. A major outstanding question is whether the deposited ferromagnetic metals enter the pores during deposition or do the pores simply modify the overlying films' roughness? Variable energy positron techniques were used to study both the morphology of the Co-film and the nano-porosity of the porous silicon samples. The measurement scheme is indicated in Figure 34.

Two types of porous silicon samples were prepared with differing porosities and film thicknesses:

- Porous Si **(M1-XS0111)**: porosity 83%, 989 nm pSi/Si substrate, 15% HF, 12 mA/cm^2, 137 seconds
- Porous Si (**M4-XS0110**): porosity 76%, 1034 nm pSi/Si substrate, 15% HF, 2 mA/cm^2, 822 seconds

The thickness and average porosity were determined by optical reflectance.

Figure 35 shows the S-parameter vs. incident energy for both porous silicon samples, with the limit of the S-parameter at 511 keV ± 0.76 keV. The spectra show a higher S-parameter in the porous layer below 5 keV and a lower value in a deeper layer above 10 keV representing the Si substrate. The high S-parameter in the porous layer is attributed to positrons annihilating with low-momentum valence electrons surrounding the pores. For both samples, in the energy range below about 4 keV, the S-parameter increases with increasing energy which is attributed to increased back-diffusion of positronium into the vacuum for positrons implanted in the near surface region. Alternatively, this could be due to the suppression of Ps formation due to a decrease in the number of spur electrons produced at lower incident energies.

The self-annihilation of *o*-Ps , measured for the first time, was characterized by the *V/T* parameter which indicated large pore size increases the probability of 3γ-annihilation giving rise to an

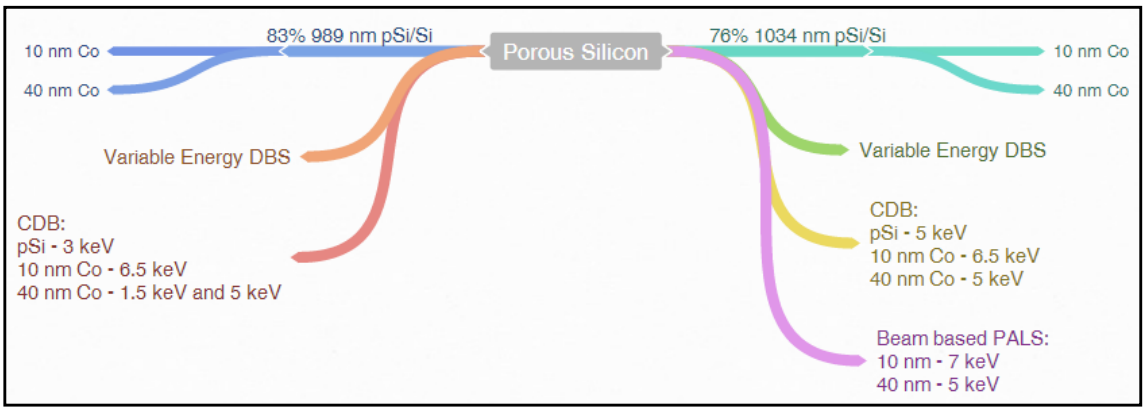

Figure 34: Porous silicon experiments at the University of Tsukuba and Science Technology Institute.

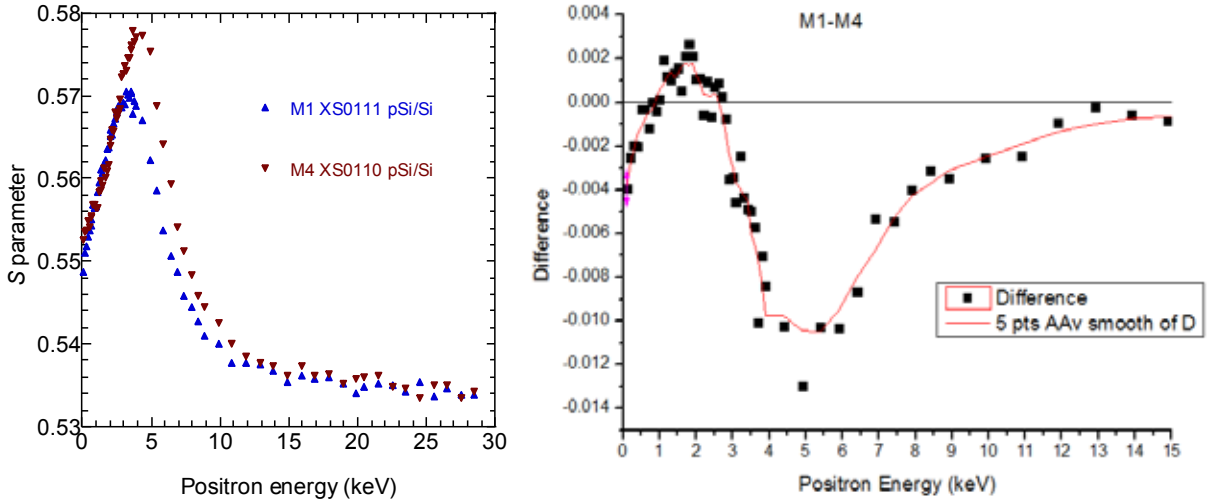

Figure 35: Left: S-parameter vs. Energy plot for the M1 and M4 samples; right: difference, M1-M4, as a function of positron energy for the two samples.

increase in the *V/T* value, as o-Ps 3γ-annihilation produces a continuous energy distribution from 0–511 keV. Also the observed *V/T* versus positron energy relationship for pSi was typical for an open pore structure, indicating that Ps formed in the film diffuses out from the sample, and annihilates in vacuum via the 3γ-annihilation process. Both the S-parameter and *V/T* depth profiles indicate that sample XS0110 has a higher porosity. These results were contrary to the total porosity predicted by reflectance measurements which gave a lower porosity for XS0110. Contamination of the samples could be an issue, especially for these highly porous materials; water diffusing into the pores will lead to a reduced S and *V/T* parameter. In future studies, porous samples will be capped very soon after fabrication.

The presence of a Cobalt layer has a significant influence on all the measured spectra. Figure 36 and Figure 37 show the S-parameter vs. Energy and *V/T*-parameter vs. Energy plots for all samples studied.

When Cobalt is deposited on the surface the measurements show both the S and *V/T* values decreased significantly; at about 5 and 7 keV the spectra coincide with pSi for the 10 and 40 nm films respectively. The reduction in S and *V/T* can be attributed to the significantly lower S-parameter for Co and the absence of Ps formation in the Co film. The reduction is therefore larger for the thicker Co film. For less than around 1 keV for the 10 nm film and 2 keV for the 40 nm film, both S and *V/T* decrease with increasing energy. This is due to the contribution from the surface state which gives rise to a higher S-parameter. The *V/T* values at the minima are almost identical to the Si substrate which exhibits no Ps formation.

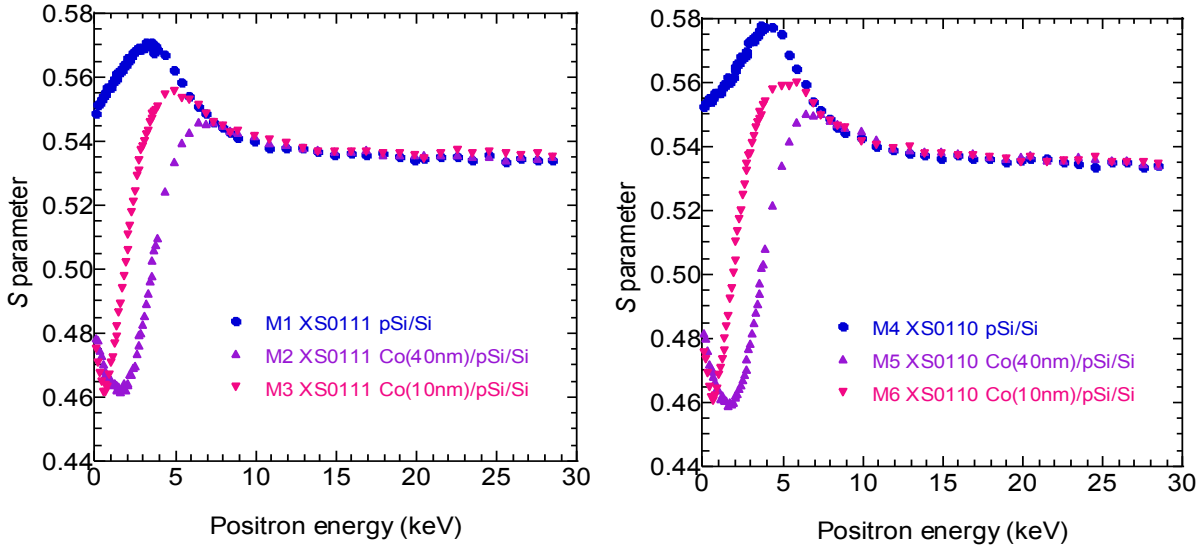

Figure 36: S-parameter vs. Energy for XS0111 (M1) and XS0110 (M4), with 40 and 10 nm of Co deposited on the surface.

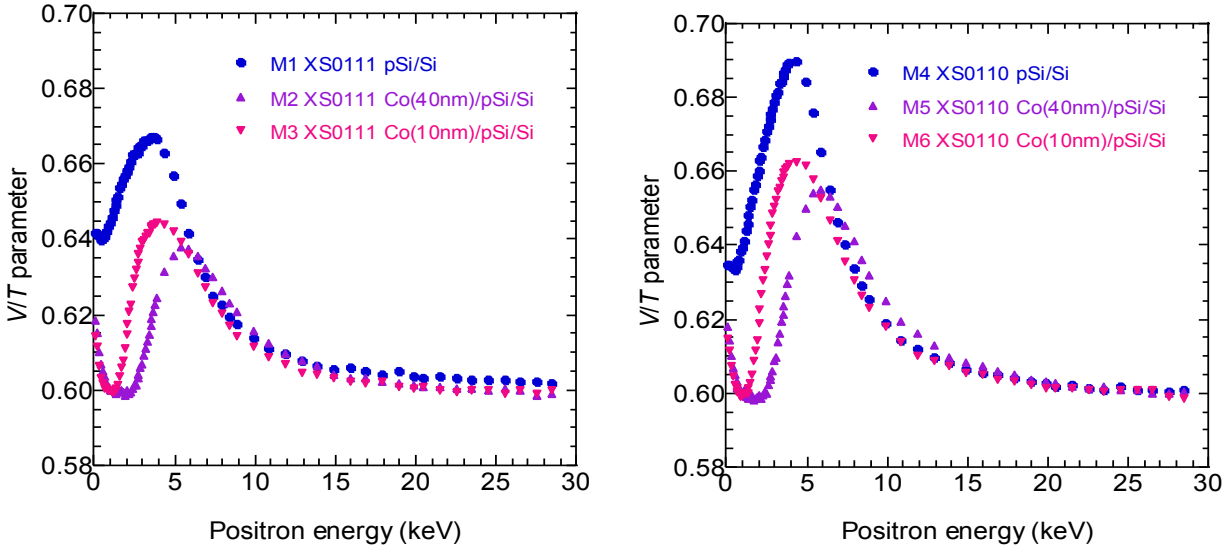

Figure 37: V/T-parameter vs. Energy for XS0111 (M1) and XS0110 (M4), with 40 and 10 nm of Co deposited on the surface.

Coincidence Doppler Broadening (Figure 38), using positrons implanted at 1.5 keV, annihilate mainly in the Co layer, as shown in the implantation profile of Figure 39. Hence the corresponding Doppler Broadening profile can be attributed mainly to positron annihilation with the electrons of the Cobalt ions. The peak observed at 1–2 momentum units is due to the annihilation of positrons with the core electrons and is suppressed at higher incident energies due to reduced overlap with the Co layer. The need for implantation profiles to complement CDB spectra for multi-layer samples, as a routine analysis procedure, is clear.

Lifetime measurements were performed at the AIST pulsed positron beamline, for samples M5 and M6 at 5 and 7 keV respectively, with the fitting results shown in the tables below.

The lifetimes are comparable; however, I_4 is larger for the 40 nm Co film sample at 5 keV. The long lifetime component, ~ 35 ns, corresponds to a 2.9 nm pore diameter using the RTE model. These measurements indicated the strength of the variable energy method and its necessary use for multilayer samples, as required for the hydrogen absorption in Pd study.

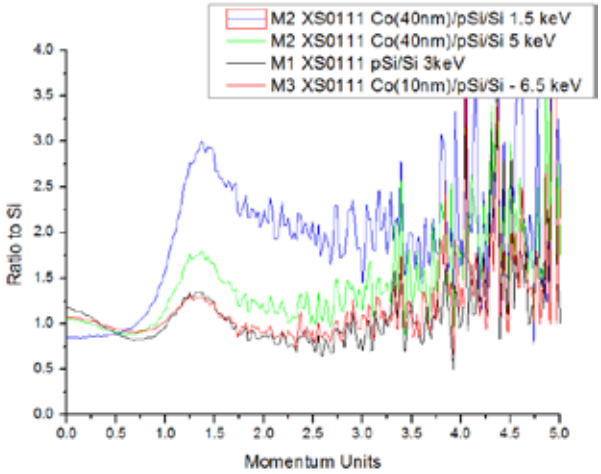

Figure 38: Momentum distribution curves for pSi and Co/pSi, as measured using CDB.

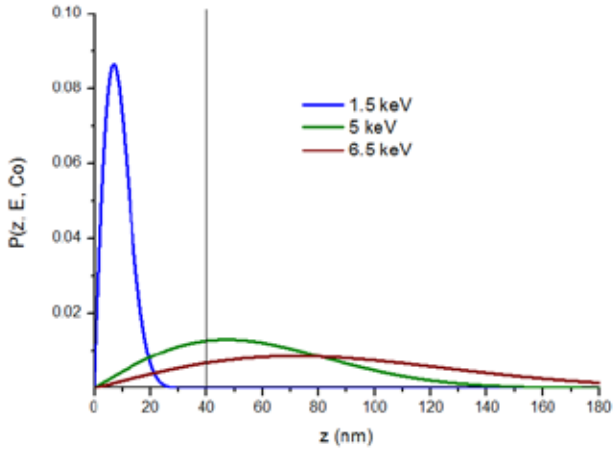

Figure 39: Positron implantation into Co results.

M6 (10 nm) at 7 keV				
Lifetimes (ns) :	0.1669	0.3861	2.0487	35.8226
Std deviations:	0.0095	0.0054	0.0931	0.6928
Intensity (%):	36.3587	57.0842	1.8481	4.7091
Std dev:	1.8056	1.7433	0.0859	0.0356

M5 (40 nm) at 5 keV				
Lifetime (ns):	0.1677	0.3964	2.0154	35.3537
Std dev:	0.0115	0.0060	0.0899	0.5688
Intensity %:	31.8633	58.6436	2.4030	7.0901
Std dev:	1.8373	1.7546	0.1114	0.0439

Hydrogen in palladium

Hydrogen absorption by Pd changes the magnetic properties of a Pd/Co bi-layer due to variation in the magnetic anisotropy of the Co layer due to an interface effect and has applications in H_2 sensing. As shown in Figure 40, three types of Pd samples were investigated, with and without H_2 exposure, in this study. Positron annihilation revealed the structure of the film/interface due to hydrogen dosing. Absorption of H_2 above a critical concentration is known to lead to the formation of palladium hydride phase (β phase), leading to irreversible plastic deformation . This can cause stability problems when using Pd films for hydrogen sensing. Variable-energy Doppler broadening was employed for this investigation.

Many measurements were made of these samples and characterized as follows. The S-parameter was found to decrease with increasing thickness of Pd, due to reduced overlap with the Si substrate which displays a higher S-parameter.

In Figure 41 the S vs. E curves for the three types of samples are compared with and without hydrogen dosing. A small difference in the curves is seen for the 100 nm Pd film indicating some plastic deformation. On the other hand, the thinner films do not show significant change, indicating that these films will be stable as hydrogen sensors. Small differences at low energies could be the result of surface contamination. Future work includes VEPFIT modeling, comparison with magnetic measurements and variable hydrogen exposure. The present proof of principle study supported the further extended measurements with this technique.

The quantum nature of hydrogen in materials became apparent during this study. Unresolved issues relate to hydrogen bonding, hydrogen induced properties such as magnetism embrittlement, thermal conductivity and in particular absorption and desorption mechanisms on material surfaces. Quantum beams such as neutron scattering (observing the proton of hydrogen but not the electron), X-ray (observing electrons but not protons) and muon beams (observing excited states of hydrogen) will provide new data on the position of the hydrogen atoms, and the bonding of hydrogen with surrounding atoms, for example. This work indicated our initial and successful collaborative studies with CMRC, Tsukuba, Japan.

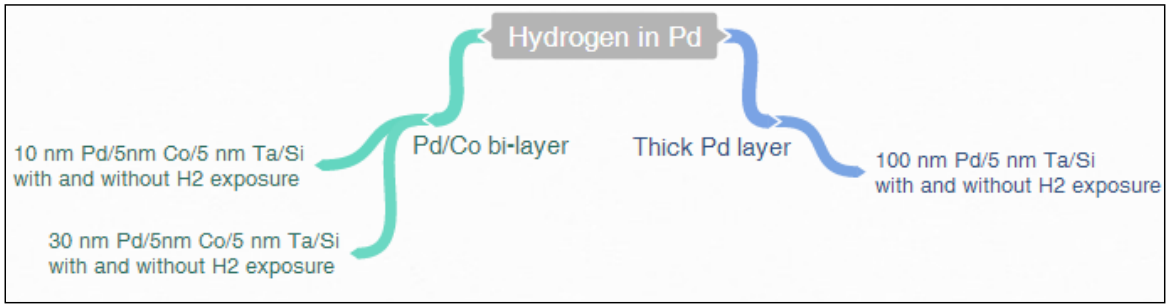

Figure 40: Three types of palladium samples were studied with and without H_2 exposure.

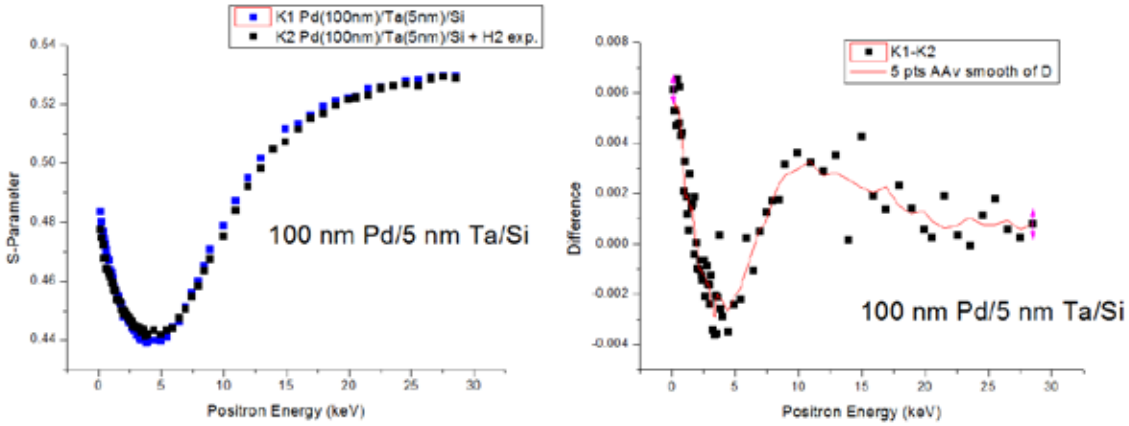

Figure 41: Variations of the S-parameter versus positron beam energy for 100 nm Pd/5 nm Co film on Si substrate, with and without hydrogen exposure.

Experimental facilities

The papers published this year from the UWA Node used their access to a wide range of probing facilities either within the UWA Node, the UWA CMCA (Centre for Microscopy and Microanalysis), the ANSTO laboratories, the University of Mysore Department of Physics (PALS), and the University of Tsukuba.

Most notable is the UWA slow positron beam facility which has been in operation for about three years. A sealed 6 mCi UHV ^{22}Na source provides a longitudinally polarized positron beam which is electrostatically transported along a magnetic free path, and then turned though 90˚ into a surface science UHV chamber with normal surface characterizing instruments. Two 50 mm microchannel plates can detect either scattered positrons or ejected electrons from a surface. A wide range of energy and angle dependent measurements have been made, both in transmission and reflection, of positrons and of ejected electrons. Highlights of our facilities include:

- A mini-Mott electron spin detector is attached to the electron-pair surface experiment, and to the SEM, to provide the first Australian instrument with spin analysis of the scattered and ejected electrons.
- X-ray diffraction with Cu(Kα) radiation uses a Bruker instrument.
- The SEM, either at UWA or ANSTO, has been used; the former is an early model JEOL and the latter is a Zeiss Ultra Plus instrument with an attached Oxford Instrument X-Max 80 mm SDD X-ray microanalysis system.
- The PALS apparatus is a fast-fast coincidence spectrometer consisting of a BC418 plastic scintillator (Saint-Cobain Crystals) coupled to a Burle 850 photomultiplier.
- The CDB system provides elemental characterization using a BaF_2 detector and a high purity HpGe detector, with 1.1 keV full-width-at-half-maximum of the 662 keV γ-line of ^{137}Cs radioactive source.

- The UWA spin-polarized electron source uses a10mW circularly polarized laser for photoemission from a GaAs source, strained or unstrained, to deliver up to a 68% polarized electron beam.
- A 4 x 10^{-11}Torr surface analysis system contains electron-pair instrumentation including LEED, Auger, PLEED, ion beam and evaporative atom sources, and a residual gas mass spectrometer analyzer.

Interaction of low energy positrons with surfaces

We continue studying the interaction of low energy positrons with surfaces, and this study can be subdivided into the following categories:

1. Probing positron states in a solid.
2. Scattering of very low-energy positrons from a potential step-up at the sample surface.
3. Re-emission of positrons as a function of the incident positron energy.
4. Diffraction of positrons and generation of secondary electrons by low-energy positrons.

Probing positron energy structure of a solid surface

We have developed a new positron spectroscopy of surfaces approach based on scattering of very low energy positrons, in order to study the energy distribution of positron states in a solid. When a low energy positron enters a solid it occupies an empty "positron" state above the vacuum level. The spectrum of unoccupied positron states, in general, is different from the electron unoccupied states. The energy distribution of positron states above the vacuum level and the general knowledge of the positrons' properties are important for the interpretation of the variable energy PALS data.

Indeed, the annihilation of a positron inside a solid follows an implantation of a positron at a certain depth inside the solid. Elastic scattering of a positron back into the vacuum is a competing channel to the implantation. On the other hand, one can expect that the probability of a positron scattering back into the vacuum (that is complementary to the probability to enter the solid) is sensitive to the density of positron states at the corresponding level (these states are of course unoccupied): the reflectivity is high where the density of states is small or where the energy gap exists. In contrast, the reflectivity is small where the density of states is large. This probability is also sensitive to the shape of the surface potential barrier.

In the case of electrons there is a very efficient technique for studying unoccupied states above the vacuum level, involving elastic and inelastic scattering of electrons from a surface. This technique is named Total Current Spectroscopy (TCS) [21], or sometimes it is also called Very Low Energy Diffraction [22]. The principle of TCS is represented by Figure 42.

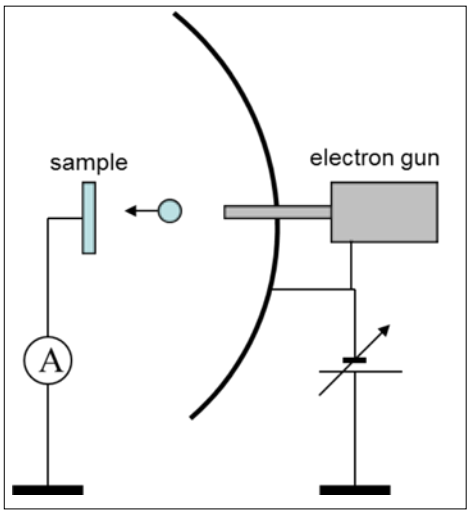

Figure 42: Experimental set-up for Total Current Spectroscopy with electrons.

In this technique one measures an electron current through the sample, I_S. The balance between the incident current I_O, reflected I_R and sample current I_S, at various potentials V applied between the sample and the electron source, is described by:

$$I_O(V) = I_S(V) - I_R(V), \qquad (1),$$

where the minus sign takes into account the direction of the current. Assuming that the incident current I_O does not depend on the V (in some range of variation in V), and taking a derivative of both sides of (1), we will have:

$$dI_S/dV = dI_R/dV \qquad (2).$$

This means that when we measure the current flow through the sample by the meter A, we measure at the same time the electron reflection as a function of the electron energy. The measured electron reflectivity contains information on the unoccupied electron states, on the band gaps and on the details of the surface potential barrier [21,22].

It is obvious that in the case of a positron primary beam an analogue technique can be applied, for studying the positron density of states as well as the surface potential barrier seen by positrons.

Technically, it is much more convenient to measure scattered positrons instead of measuring the positron current through the sample. The experimental set-up for measuring the number of scattered positrons as a function of the incident positron energy is shown in Figure 43.

The retarding field analyser (left panel of Figure 43) consists of a micro-channel plate detector (50 mm in diameter) and two grids in front of the detector. When we select the central part of the detector, the retarding curve represents only the paraxial part of the re-emitted positrons and therefore is

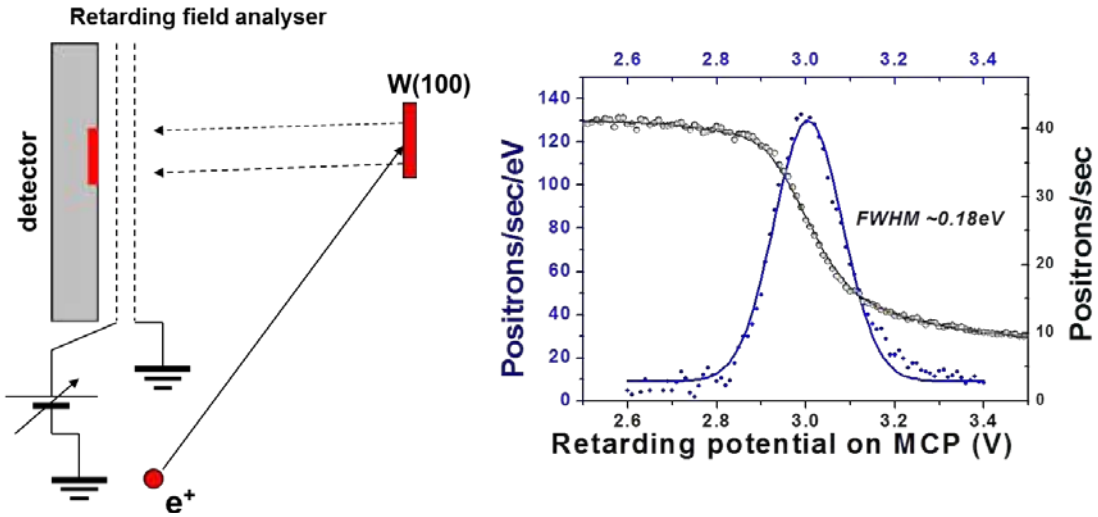

Figure 43: Retarding field analyser for measuring the energy distribution of scattered positrons (left) and an example of the energy distribution of re-emitted positrons from W(100), E_p = 250 eV (right).

rather narrow (see right panel of Figure 43). In our measurements of the reflected positrons we used the full area of the detector.

We have measured the number of scattered positrons from a W(100) surface (as well as from thin Ni films deposited on W(100)) as a function of the moderator potential, which determines the incident positrons energy. Given the W(100) sample has a negative work-function of about 3 eV, a positron approaching the sample surface with an energy say 1 eV above the vacuum level will see a step-like potential and will be reflected. When the energy of incident positrons increases up to the positron work-function they start entering the solid and, by consequence, this reduces the reflection of positrons from the surface. The energy dependence of the positron reflectivity at higher energies is likely related to the density of positron states distribution above the positron work-function level. The measured spectra are very sensitive to the surface conditions of the sample: they change after surface oxidation or thin film deposition.

Figure 44 shows the positron reflectivity curves for clean and oxidized surfaces of W(100). First of all one can see the very good reproducibility of the measurements. Indeed, the red and black curves are measured on a clean W(100) surface before and after the oxidation of the surface, whereas the blue curve corresponds to the oxidized surface. One can see that the oxidation of the surface dramatically changes the positron reflectivity curve. The first maximum at about -2 Volts of the moderator potential is present in all curves, and corresponds to the high reflectivity of positrons from the step-up barrier. However, at a moderator potential of about zero, the positron reflectivity drops down corresponding to the fact that positrons then can enter the surface above the work function barrier. Up to this potential the curves for the clean and oxidized surface are very similar. For a higher moderator potential the curve for the oxidized surface declines from the curves corresponding to the clean W(100) surface. This indicates that the oxygen adsorption (and oxidation) changes substantially the available positron states in the surface region of the sample.

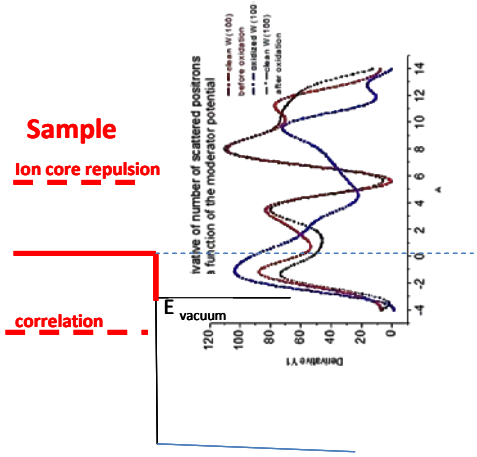

Figure 44: Reflectivity of low-energy positrons as a function of their energy. Blue curve shows reflectivity of W(100) covered by oxygen atoms. Black curve shows reproducibility of results measured after the oxygen was removed.

Scattering of very low-energy positrons from a potential step-up at the sample surface

We have observed the re-emission of positrons from a W(001) surface at various primary energies. The remaining question was: how does the positron re-emission behave at very low incident energy (close to zero). First, we measured the energy distribution of positrons scattered from

the sample when the moderator potential is lower than the sample potential. Given our moderator is a tungsten foil and the sample is a W(001) crystal, we assume the energy diagram in this case can be represented by Figure 45. The moderator is biased by -2 Volts with respect to the sample. This means that the positrons which escaped from the moderator and are transported to the sample surface will face the step-up barrier at the sample surface. They have no chance to penetrate into the sample and must be reflected back into the vacuum, unless they are trapped by surface image-states and annihilated with electrons from the electron cloud near the surface. In this case the energy distribution of the scattered positrons is determined only by their energy distribution in the incident beam. When the moderator bias reaches zero, or becomes positive with respect to the sample, the positrons from the moderator can enter the surface and then they may be re-emitted. Alternatively they can be reflected from the surface. This means, when we detect back scattered positrons, there is a fraction of re-emitted and a fraction of reflected positrons. The energy distribution of the positrons scattered from the potential barrier (left curve of Figure 46) and re-emitted (right curve of Figure 46), have different FWHM as indicated on the figure. As expected, the energy distribution of positrons scattered from a potential barrier is determined by the energy spread of the incident positron beam, 0.7 eV, that was also measured in a separate experiment. The energy distribution of the re-emitted positrons is more narrow, 0.4 eV, and is determined by the distribution of thermalized positrons and their angular distribution.

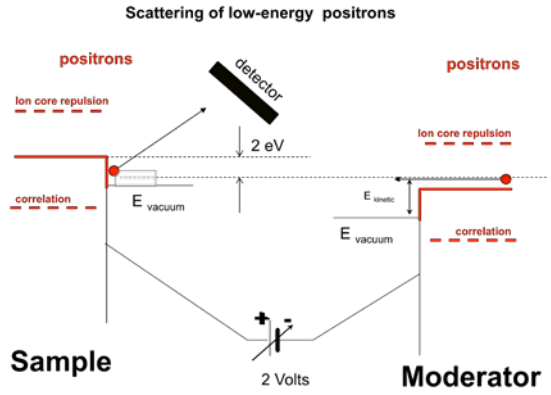

Figure 45: Energy diagram for low energy positron scattering from W(001). The moderator is biased by -2 Volts with respect to the sample.

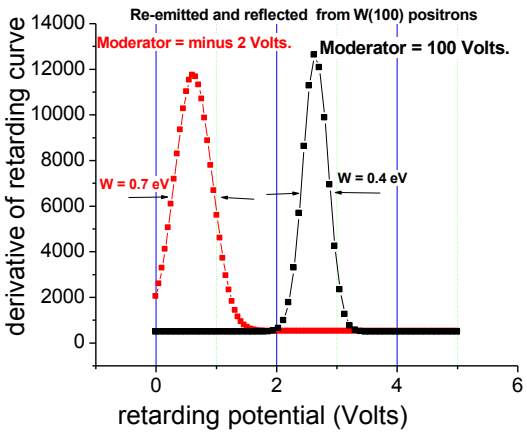

Figure 46: Energy distribution of positrons scattered from a potential barrier (left) and re-emitted (right).

Re-emission of positrons from W(001) as a function of primary energy

The re-emission yield of thermalized positrons, as a function of their incident energy, was studied for Cu(110) in the energy range 0–40 eV [23]. The various competing interactions at these low energies still need to be identified and characterized.

We also performed such measurements on W(001). When positrons are incident on materials such as tungsten, which have a negative work function, a fraction of the thermalized positrons are re-emitted with energies equal to the work function of the material. We have measured this thermalized positron re-emission yield from W(001) in a direction normal to the surface for the incident positrons energies up to 60 eV (Figure 47). The re-emission yield increased with incident positron energies, similar to that reported by Baker et al., but surprisingly was lower for incident energy positrons in the range 22 to 29 eV.

The specular scattering of positrons has also been measured and is shown in Figure 48. A large maximum around 15–16 eV is observed, as expected for diffraction from the crystal surface of W(001). Since the incident angle of the positron for the re-emission yield measurements was 45˚ (as restricted by our experimental system), the expected elastic scattering maximum was about 26 eV, which corresponds with the lower re-emission yield at these energies (see Figure 47). These studies strongly suggest that elastic scattering, as a competing channel, is responsible for the structure in the re-emission yield.

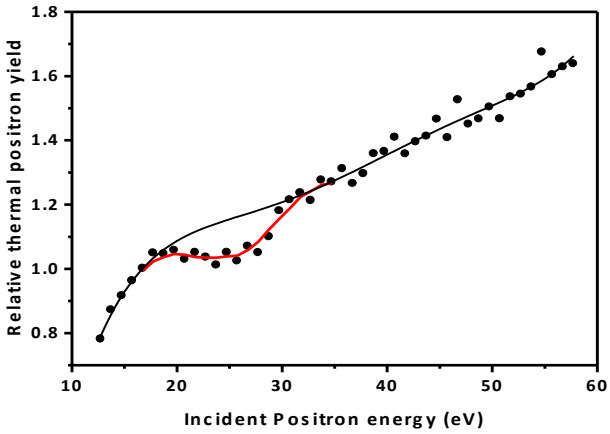

Figure 47: Re-emission yield of thermal positrons as a function of their incident energy.

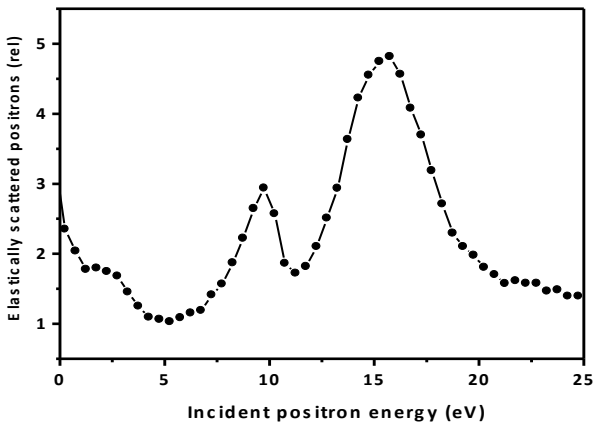

Figure 48: Elastic scattering of positrons from W(001) at a specular geometry, scattering angle 67.5˚.

Diffraction of positrons and generation of secondary electrons by low-energy positrons

In order to investigate the mechanism of secondary electron generation from W(001), by the positron impact, we studied the electron yield as a function of the primary positron energy in the energy range where a diffraction of positrons is observed. Figure 49 represents the positron scattering probability as a

function of the primary positron energy (black dots), as well as the elastic positron scattering as a function of primary positron energy (open red dots). One can see a clear diffraction pattern at about 16 eV. A low-energy maximum at about 10 eV is not identified and may be due to multiple positron scattering on the surface potential barrier. The intensity of the electron emission as a function of the positron primary energy is shown by red bold dots.

One can see a maximum on this curve at about 16 eV (or 13 V moderator potential), that coincides with the diffraction maximum of the positron scattering probability curve. This feature indicates that a substantial number of electrons are generated by the diffracted positrons and that these electrons are generated by positrons that underwent first diffraction on the W(001) crystal. Since the electron and positron curves do not look identical, some number of electrons is generated in alternative channels. For example, an incident positron first excites an electron (that can escape) and after that it either annihilates or scatters back into the vacuum.

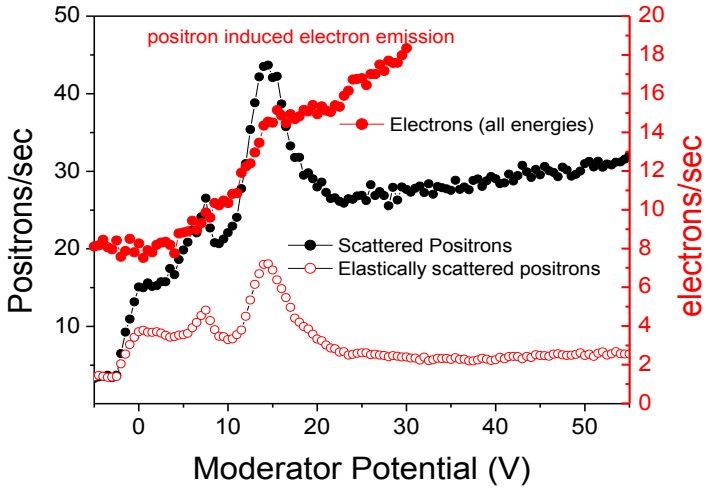

Figure 49: Positron scattering probability as a function primary positron energy (black dots); Positron elastic scattering probability as a function primary positron energy (red open dots); electron emission intensity as a function of the primary positron energy (filled dots).

Interaction of spin-polarized electrons with surfaces

We continued the study of thin ferromagnetic layers on a nonmagnetic substrate, using spin-polarized single- and two-electron spectroscopy. Spin-polarized electron energy loss spectroscopy (SPEELS) provides information on the magnetic state of the sample, in the form of the Stoner excitation asymmetry. It turns out that the magnitude and shape of the spin asymmetry from SPEELS, depends on the kinematics of scattering as well as on the magnetic state of the sample.

Influence of kinematics on the Stoner excitation asymmetry

We have measured the intensity asymmetry of SPEELS for a 5 ML Fe film on W(110), at the two different geometrical arrangements depicted in Figure 50: a) normal incidence and detection of electrons at 50˚ with respect to the sample normal; b) specular geometry with the angle of incidence at 25˚ and the detection angle at 25˚. The asymmetries of the energy loss spectra measured in the two different geometries are shown in Figure 50 (overleaf). The maximum absolute values of the Stoner excitation asymmetry at normal incidence and at the specular reflection at 25˚ are almost the same, but the shapes of the asymmetry spectra are different. At specular reflection the asymmetry changes sign at about 14 eV and there is a distinct kink at 5 eV energy loss. At the same time the asymmetry of the elastic maximum significantly